# Monolithic 3D-printed slotted hemisphere resonator bandpass filter with extended spurious-free stopband

Li, Jin; Li, Sheng; Huang, Guan Long; Yuan, Tao; Attallah, Moataz M.

*DOI:*
10.1049/el.2018.7850

Date of publication xxxx 00, 0000, date of current version xxxx 00, 0000.

*Digital Object Identifier 10.1109/ACCESS.2017.Doi Number*

# 3-D Printed Slotted Spherical Resonator Bandpass Filters With Spurious Suppression

**Fan Zhang[1], Sufang Gao[2], Jin Li[3], Member, IEEE, Yang Yu[4, 6], Cheng Guo[4, 7], Sheng Li[5], Moataz Attallah[5], Xiaobang Shang[8], Senior Member, IEEE, Yi Wang[4], Senior Member, IEEE, Michael J. Lancaster[4], Senior Member, IEEE, and Jun Xu[1]**

[1]School of Physics, University of Electronic Science and Technology of China, Chengdu, Sichuan 610054, China
[2]Xi'an Microelectronics Technology Institute, Xi'an, Shaanxi 710065, China
[3]Guangdong Provincial Mobile Terminal Microwave and Millimeter-Wave Antenna Engineering Research Center, College of Electronics and Information Engineering, Shenzhen University, Shenzhen, Guangdong 518060, China
[4]Department of Electronic, Electrical and Systems Engineering, University of Birmingham, Edgbaston, Birmingham B15 2TT, U.K.
[5]School of Metallurgy and Materials, University of Birmingham, Edgbaston, Birmingham B15 2TT, U.K.
[6]Department of Electrical and Electronic Engineering, Southern University of Science and Technology, Shenzhen, Guangdong 518055, China
[7]Department of Information and Communication Engineering, Xi'an Jiaotong University, Xi'an, Shaanxi 710049, China
[8]National Physical Laboratory, Teddington, Middlesex TW11 0LW, U.K.

Corresponding author: Sufang Gao (sufangg@yahoo.com).

This work was supported by the U.K. Engineering and Physical Science Research Council under Contract EP/M016269/1. The work of F. Zhang was supported in part by the China Scholarship Council under the State Scholarship Fund.

**ABSTRACT** In this paper, a third-order waveguide bandpass filter (BPF) based on slotted spherical resonators with a wide spurious-free stopband is presented. The resonator consists of a spherical cavity with slots opened at the top and bottom. Compared with a non-slotted spherical resonator, the slotted resonator suppresses the two spurious modes ($TM_{211}$ and $TE_{101}$) whilst maintaining the fundamental $TM_{101}$ mode. The unloaded quality factor of the $TM_{101}$ mode is not significantly degraded. This is achieved by interrupting surface current and radiating the unwanted spurious modes with the slots. The BPF is designed at a center frequency of 10 GHz with a fractional bandwidth of 1%. Two filter prototypes are fabricated one by using metal-based selective laser melting (SLM) and the other by polymer-based stereolithography apparatus (SLA) techniques. The slots also facilitate the copper electroplating process for the SLA-printed filter. The measured result shows that the average passband insertion losses of the SLM- and SLA-printed filters are 0.33 and 0.2 dB, respectively. The corresponding passband return losses are better than 22 and 20 dB. The filters demonstrate excellent passband performance and wide spurious-free stopbands up to 16 GHz with stopband rejections of over 20 dB.

**INDEX TERMS** Bandpass filter, selective laser melting, slotted spherical resonator, spurious suppression, stereolithography apparatus, 3-D printing.

## I. INTRODUCTION

Microwave resonators are the building blocks of passive microwave devices such as filters and multiplexers. Rectangular and cylindrical resonators [1]–[3] have been widely used because they can be readily fabricated by using conventional manufacturing technologies. In recent years, additive manufacturing, also known as 3-D printing, has been reported in the fabrication of microwave devices. Complex geometries can be 3-D printed to enhance the performance of microwave devices [4]–[15]. A good example is the 3-D printed spherical resonator with intrinsically high unloaded quality factor ($Q_u$). In [4] and [5], spherical resonators were 3-D printed to construct waveguide bandpass filters (BPFs). The BPF in [4] exhibited a very low passband insertion loss (IL). However, the spherical resonator suffered from spurious modes spectrally close to the fundamental mode. This degraded the stopband performance of the filter. The stopband rejection was improved by using the 90°-twisted coupling geometry in [4] to minimize coupling strength of the spurious $TM_{211}$ mode. Another example is the mathematically defined super-ellipsoid resonators presented in [6] and [7] showing excellent filtering performance. However, except for [6] and [7], there has been little work in spurious suppression for the filters.

In this work, we focus on improving the spurious-free region of the spherical resonator BPFs. A new approach aiming to maximize the spurious suppression through slotting the cavities is presented. The spurious $TM_{211}$ and $TE_{101}$ modes of the spherical resonator are effectively suppressed without compromising the high $Q_u$ of the fundamental $TM_{101}$ mode. This significantly enlarges the spurious-free stopband. This is achieved by interrupting surface current of the spurious modes with slots. The slots are appropriately arranged on the cavity shells to ensure that the spurious $TM_{211}$ and $TE_{101}$ modes are suppressed and the $TM_{101}$ mode is not disturbed. The proposed method of slotting for spurious resonance suppression significantly enhances the spurious-free region as compared to the filter in [5]. Application of the proposed slotting method is possible for other types of air-filled cavity resonators. In the following sections, a third-order waveguide BPF based on slotted spherical resonators will be demonstrated.

## II. SLOTTED SPHERICAL RESONATORS

When an air-filled spherical resonator is fed with a rectangular waveguide, as demonstrated in [4], the first and second excited spurious modes are $TM_{211}$ and $TE_{101}$ modes. With a fundamental mode ($TM_{101}$) at 10 GHz, the resonant frequencies of the $TM_{211}$ and $TE_{101}$ modes are 14.08 and 16.39 GHz, respectively. The surface current distributions of these modes are illustrated in Fig. 1. In order to suppress the spurious modes, a rectangular slot in the spherical cavity, as illustrated in Fig. 2(a), is proposed. The suppression is realized by interrupting surface current of the spurious modes with the slots, so these modes radiate. As can be seen from Fig. 1 and Fig. 2(a), the slots are along the directions parallel to the $TM_{101}$-mode surface current, but intersect the currents of the spurious modes. In addition, the slots are placed in the region with a low current density for the fundamental mode, but relatively large current densities for the spurious modes. Therefore, the $TM_{211}$ and $TE_{101}$ modes are suppressed through radiation without significantly interfering with the $TM_{101}$ mode. This is verified by investigating the responses of the resonator model in Fig. 2(a). The transmission coefficient ($S_{21}$) obtained from electromagnetic (EM) simulation in CST [16] is plotted in Fig. 2(b). It is shown that the spurious resonances at 14.08 and 16.39 GHz have been effectively eliminated after the slots are introduced whilst the $TM_{101}$-mode resonance is not affected. It should be mentioned that the spurious $TM_{311}$ mode at 18.08 GHz has a similar current distribution with the $TM_{101}$ mode. So, suppression of the $TM_{311}$ mode and others beyond without affecting the $TM_{101}$ mode can be difficult.

EM-simulated transmission responses of the slotted spherical resonator under different slot dimensions are graphically compared in Fig. 3. The results show that the suppression level is mainly determined by the slot length *l*. As the length *l* is increased from 9 to 13 mm, the suppression of the $TM_{211}$ and $TE_{101}$ modes is significantly enhanced, as

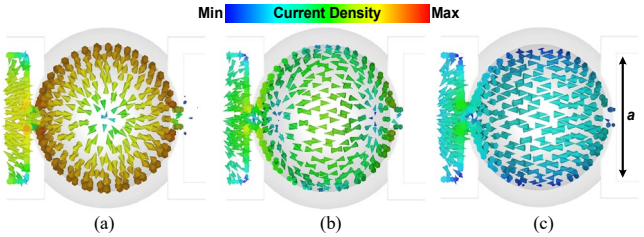


**FIGURE 1.** Simulated surface current distribution (top views) of the resonant modes in a two-port weakly coupled air-filled spherical resonator. (a) The $TM_{101}$ mode. (b) The $TM_{211}$ mode. (c) The $TE_{101}$ mode. The parameter *a* is the width of the feeding rectangular waveguide's broad wall.

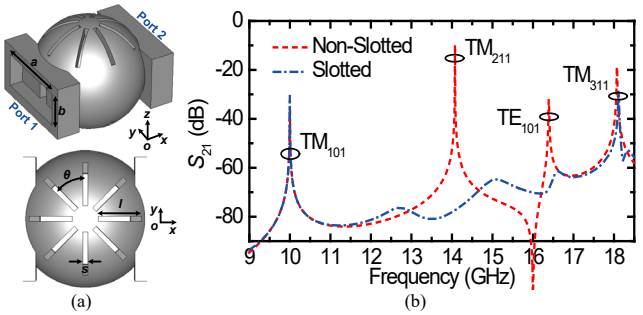


**FIGURE 2.** The slotted spherical resonator with weak waveguide external couplings. Feeding windows of 3.5 mm × 10.16 mm are used. (a) A structural illustration (upper: a 3-D view; lower: a top view). (b) EM-simulated transmission coefficient. Copper electrical conductivity of $5.96 \times 10^7$ S/m was used in the simulation for cavity boundaries. The slot dimensions are $s$ = 1.21 mm, $l$ = 11.91 mm, and $\theta$ = 45°.

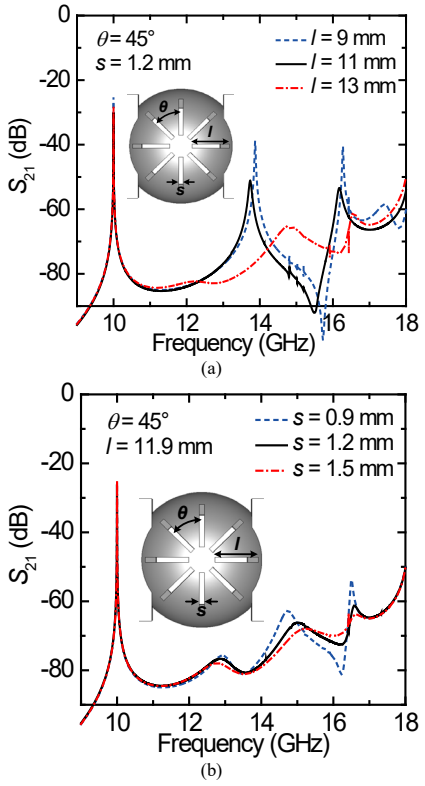


**FIGURE 3.** EM-simulated transmission responses of the slotted spherical resonator with different slot dimensions. (a) The wideband transmission coefficient versus slot length *l*. (b) The wideband transmission coefficient versus slot width *s*.

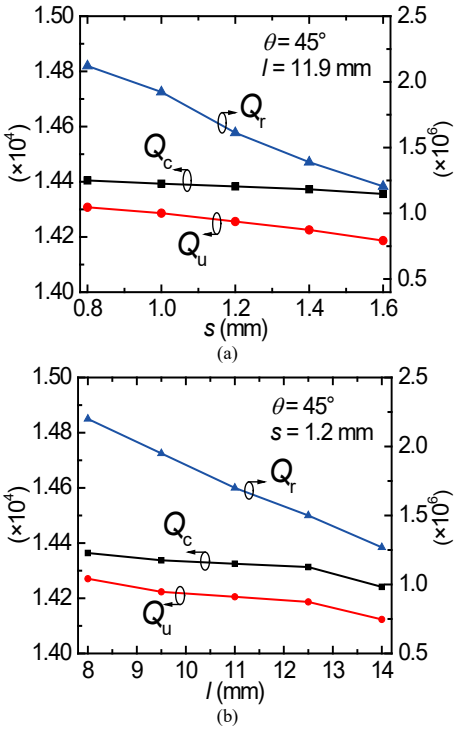


**FIGURE 4.** Simulated $TM_{101}$-mode quality factors of a slotted spherical resonator under different slot dimensions. (a) The quality factors versus slot width *s*. (b) The quality factors versus slot length *l*.

shown in Fig. 3(a). This is because in the slotted region the current for the spurious modes is concentrated and longer slots interrupt the current more effectively. The suppression is also affected by the slot width *s*, as shown in Fig. 3(b), but in a much less significant way.

It is important to quantify the influences of the slots on the $TM_{101}$-mode resonance. This is accomplished by simulations as follows. The loaded quality factor ($Q_L$) and unloaded quality factor ($Q_u$) of the slotted spherical resonator in free space can be expressed as [17]

$$Q_L^{-1} = Q_e^{-1} + Q_c^{-1} + Q_r^{-1}, \quad (1)$$

$$Q_u^{-1} = Q_c^{-1} + Q_r^{-1}. \quad (2)$$

Here $Q_e$ is the external quality factor associated with the coupling aperture between the feeding rectangular waveguide and the resonator. $Q_r$ and $Q_c$ are the radiation quality factor and conductor quality factor, respectively. We are interested in finding $Q_r$ due to the slots for the $TM_{101}$ mode and comparing it with $Q_c$. The calculation of the quality factors of the slotted spherical resonator, with $s$ = 1.21 mm and $l$ = 11.91 mm, is exemplified as follows. Firstly, to find $Q_e$ we use an unslotted spherical resonator with the coupling aperture set to be 2.5 mm by 10.16 mm. In this case, we make the material a perfect electrical conductor (PEC), hence there is no radiation loss or conductor loss. From (1) this gives $Q_L = Q_e$, which by simulation turns out to be $1.67 \times 10^7$. Now the slotted resonator is simulated with PEC, giving a value of $Q_L = 1.5 \times 10^6$. From (1) and the previously calculated $Q_e$, the $Q_r$ value can be calculated as $1.64 \times 10^6$.

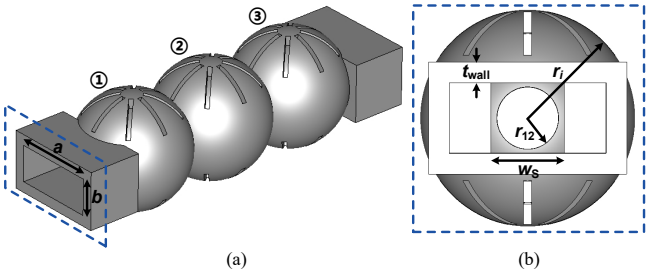


**FIGURE 5.** A geometrical illustration of the third-order *X*-band BPF based on the slotted spherical resonators. (a) A 3-D view. (b) A side view ($i$ = 1, 2, and 3 for the radius $r_i$ of the $i^{th}$ resonator, respectively).

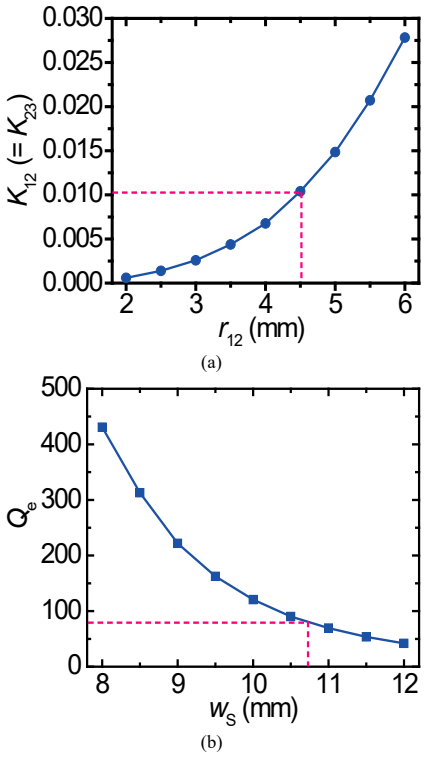


**FIGURE 6.** Extracted $Q_e$ and $K_{12}$ (= $K_{23}$) values from EM simulation. (a) $K_{12}$ (= $K_{23}$) versus $r_{12}$. (b) $Q_e$ versus $w_s$. The pink dash lines point out the required design parameters.

Next, the material is changed from PEC to copper with an electrical conductivity of $5.96 \times 10^7$ S/m and the simulation of the slotted resonator produces a $Q_L$ of $1.42 \times 10^4$. Knowing the values of $Q_L$, $Q_e$, and $Q_r$ in equation (1) allows the calculation of $Q_c$ resulting in $Q_c = 1.43 \times 10^4$. Since $Q_e$ and $Q_r$ are at least two orders of magnitude larger than $Q_c$, they have little influence on $Q_L$ in this case. It should be noted that this calculation is only an approximation, but it is good because of the large differences in the $Q$ values. It allows us to conclude that $Q_r$ has virtually no influence on the $TM_{101}$ mode as $Q_c << Q_r$. Using the calculated $Q_c$ and $Q_r$, the $Q_u$ value of the slotted spherical resonator is obtained from (2) as $1.42 \times 10^4$. This value is very close to the $Q_u$ ($1.44 \times 10^4$) of a non-slotted spherical resonator.

Using the above method, $TM_{101}$-mode quality factors of the slotted spherical resonator under different slot dimensions

TABLE I
CRITICAL DIMENSIONS OF THE DESIGNED *X*-BAND BPF (UNITS: MM)

| $a$ | $b$ | $w_S$ | $r_{12}$ | $r_{23}$ | $r_1$ | $r_2$ | $r_3$ | $t_{wall}$ | $s$ | $l$ |
|---|---|---|---|---|---|---|---|---|---|---|
| 22.86 | 10.16 | 10.73 | 4.56 | 4.56 | 12.71 | 12.89 | 12.71 | 3 | 1.21 | 11.79 |

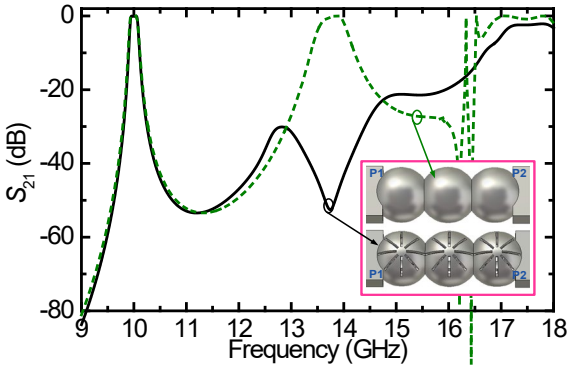


**FIGURE 7. EM-simulated wideband (*X*-to-*Ku* band) transmission responses of the BPFs. P1 and P2 stand for Ports 1 and 2.**

are calculated and plotted in Fig. 4. The simulated result shows that increasing $s$ or $l$ only reduces $Q_c$ and $Q_u$ by less than 1.5% over the inspected region of the dimension. This shows that negligible conductor loss is introduced from the enlarged slots. In contrast, $Q_r$ decreases by over 40%. However, it is still much higher than $Q_c$ (~$10^4$), indicating very little radiation loss for the $TM_{101}$ mode. From (2), it is known that the degraded but large $Q_r$ has little effect on $Q_u$.

## III. SLOTTED SPHERICAL RESONATOR FILTER DESIGN

To validate the spurious passband suppression for BPFs using the slotted spherical resonators, a third-order waveguide filter was designed. The constituent slotted spherical resonators of the filter were configured with an inline coupling geometry as illustrated in Fig. 5(a). The filter was designed with a Chebyshev transfer function with a center frequency ($f_0$) of 10 GHz, a fractional bandwidth (FBW) of 1%, and a passband return loss (RL) of 20 dB. The coupling matrix methodology was used [17]. The external quality factor ($Q_e$) and denormalized inter-resonator coupling coefficients were calculated to be $Q_e$ = 85.1 and $K_{12} = K_{23}$ = 0.0103. In the practical filter, $Q_e$ is controlled by the width $w_S$ of the rectangular coupling apertures at the source and load. The inter-resonator coupling coefficients $K_{12}$ and $K_{23}$ are controlled by the radii $r_{12}$ and $r_{23}$, respectively, as labeled in Fig. 5(b). The extracted $Q_e$ and inter-resonator coupling coefficients as a function of the dimensions are plotted in Fig. 6. The coupling strength is enhanced with the increase of $r_{12}$ and $r_{23}$, and the external coupling becomes stronger (smaller $Q_e$) as $w_S$ increases. The required design parameters can be obtained from Fig. 6 and the final dimensions of the filter is summarized in Table I. The simulated transmission response of the filter is presented in Fig. 7 in comparison with that of a reference filter with non-slotted spherical resonators of the same design specifications. It is shown that the spurious passbands of the slotted resonator filter at around 14 and 16.5 GHz are suppressed and the spurious-free stopband is greatly extended.

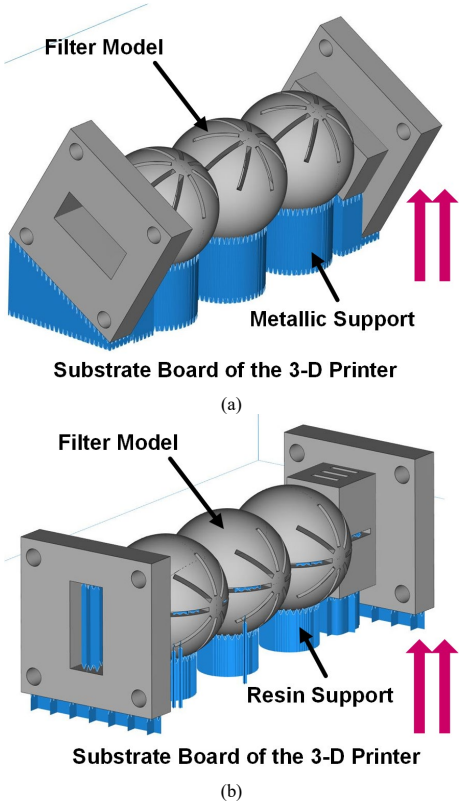


**FIGURE 8. Illustrations of the orientations of the BPF models under 3-D printing, (a) for SLM printing and (b) for SLA printing. The red arrows indicate the printing direction.**

## IV. FILTER FABRICATION

It would be very difficult to make the filter by conventional means due to the complex geometry. Therefore, additive manufacturing technology was used. To demonstrate the capability of 3-D printing, the metallic selective laser melting (SLM) and polymer-based stereolithography apparatus (SLA) were used to produce two filter prototypes.

The first prototype was SLM-printed with an aluminum-copper-based alloy (92 weight percent (wt. %) aluminum, 5 wt. % copper, and 3 wt. % others) in a powder form supplied in 15–53-μm particle size. A printing orientation, as illustrated in Fig. 8(a), was selected to ensure that no metallic support is required inside the cavities. Any internal metallic support would be very difficult to remove. After the printing process was completed, the metallic support structure outside the filter was removed manually.

The second prototype was SLA-printed with an Accura Xtreme resin [18] under a printing resolution of 50 μm. The orientation for the printing is illustrated in Fig. 8(b). For SLA, it is easier to remove resin support, so that the orientation can be selected more flexibly. After the resin

curing process, a 10-μm thick copper was electroplated onto the printed resin using the same process as in [4] and [5]. This thickness of copper was subtracted from the filter model before the 3-D

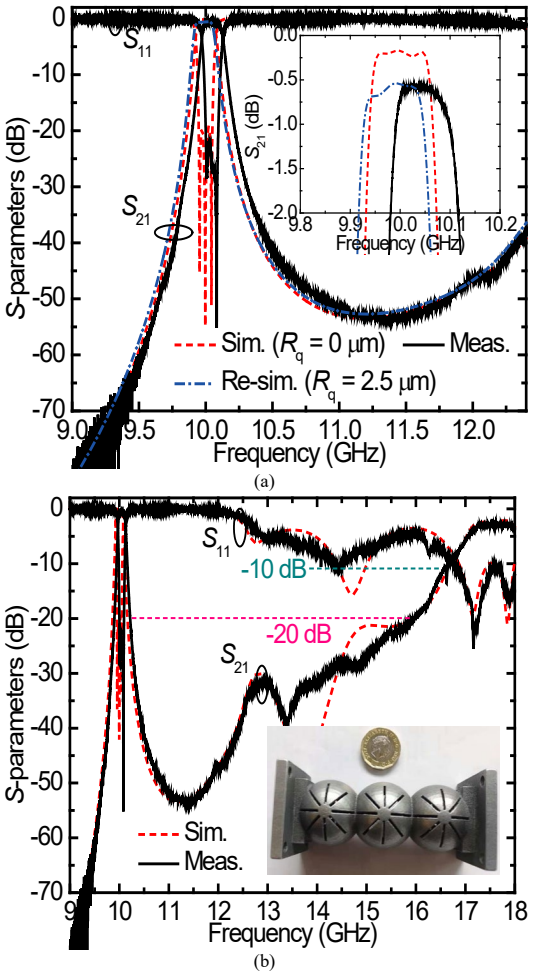


**FIGURE 9.** The SLM-printed filter (prototype I). (a) EM-simulated and RF-measured passband responses. (b) Wideband (*X*-to-*Ku* band) responses. The inset shows a photograph of the filter.

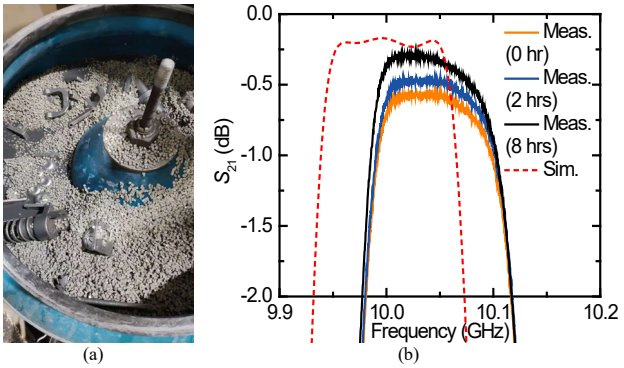


**FIGURE 10.** The surface polishing process for the metallic SLM-printed filter (prototype I). (a) Photograph of the vibration grinding machine. The grey particles are abrasive materials. (b) Passband responses of the filter before and after the polishing process.

printing by performing a structural compensation. This minimizes any frequency shift of the fabricated filter. It is very important to note that the slots on the spherical resonators are also used to facilitate the metal coating process. It can be seen from Fig. 8(b) that extra slots are cut

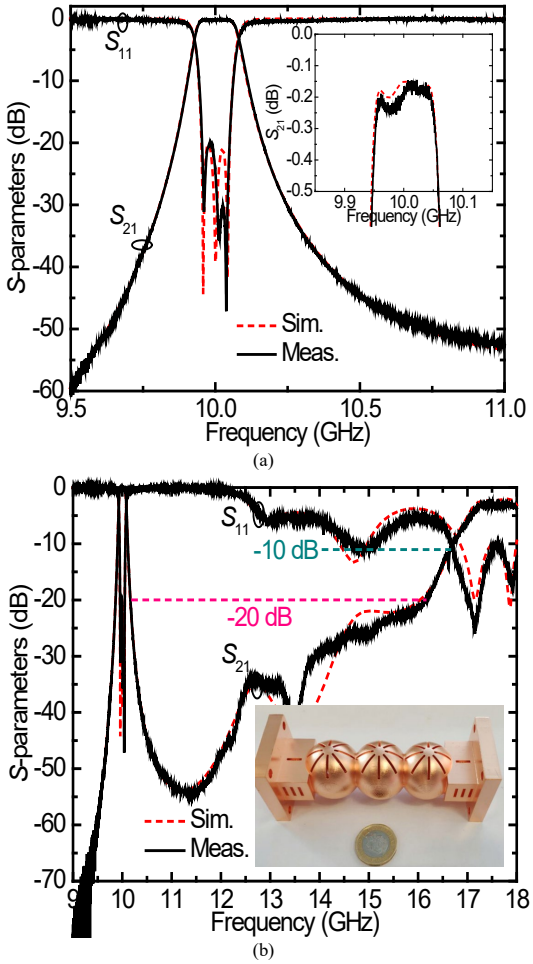


**FIGURE 11.** The SLA-printed filter (prototype II). (a) EM-simulated and RF-measured passband responses. (b) EM-simulated and RF-measured wideband (*X*-to-*Ku* band) responses. The inset shows a photograph of the filter.

through the input and output waveguide sections for the same purpose.

## V. MEASUREMENT AND DISCUSSION

The RF performance of the 3-D printed filters were measured using a Keysight network analyzer E8362C under a two-port waveguide thru-reflect-line calibration. The frequency responses at *X* and *Ku* bands were measured separately. For the *Ku*-band measurement, a pair of *X*-to-*Ku*-band waveguide tapers were used, and the network analyzer was calibrated at *Ku* band. The EM-simulated and RF-measured frequency responses of the prototype I are compared in Fig. 9, showing good agreement. The measured passband IL and RL are averagely 0.62 dB and greater than 22 dB, respectively. The IL is 0.4–0.5 dB

higher than the simulated value. Assuming the IL increment is only attributed to the surface roughness of the printed alloy, this corresponds to an equivalent root mean square roughness ($R_q$) of about 2.5 μm. The re-simulated $S_{21}$ parameter taking into account the 2.5-μm surface roughness agrees better with the measured one, as shown in Fig. 9(a).

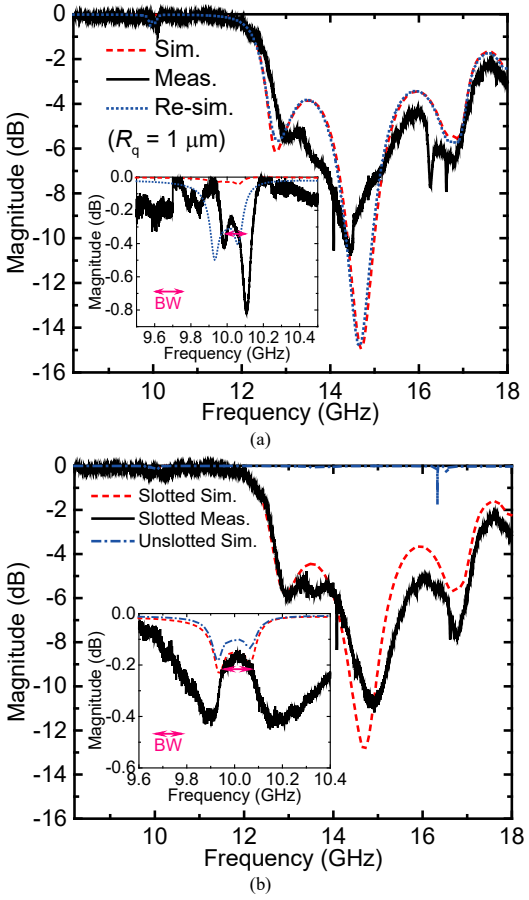


**FIGURE 12. EM-simulated and RF-measured losses (1 - $|S_{11}|^2$ - $|S_{21}|^2$) of the filters. (a) The prototype I. (b) The prototype II.**

TABLE II
COMPARISON WITH PREVIOUSLY REPORTED 3-D PRINTED BPFS

| Ref. | Res. | $f_0$ | FBW (%) | IL (dB) | RL (dB) | $\Delta f$ (%) | Spurious Suppression | $f_1/f_0$ |
|---|---|---|---|---|---|---|---|---|
| [4] | S | 10 | 5 | 0.11 | >20 | 0.05 | — | 1.32:1 |
| [5] | SS | 10 | 3 | 0.24 | >18 | <0.01 | — | 1.27:1 |
| [6] | SE | 12.875/ 14.125 | 1.94/ 1.77 | 0.2 | >18 | <0.2 | Yes (>55 dB) | >1.7:1 |
| [8] | H | 32 | 1/5 | 0.43–1 | >10–17 | <0.47 | — | 1.37:1 |
| T.W. | SS | 10 | 1 | 0.2 | >20 | 0.04 | Yes (>20 dB) | >1.7:1 |
| T.W. | SS | 10 | 1 | 0.33 | >22 | 0.5 | Yes (>20 dB) | >1.7:1 |

*T.W.: This work; Res.: Resonators; S: Spherical; SS: Slotted spherical; H: Hemispherical; SE: Super-ellipsoid; $f_1/f_0$: Frequency ratio of the first spurious passband to the fundamental-mode passband.

The measured $Q_u$ for the slotted spherical resonator is estimated to be 2830. The measured frequency shift ($\Delta f$) is about 0.5% and is caused by the volume shrinkage of the metal-printed cavities. Shrinkage is usually induced during the laser melting process because of the phase transformation and the contraction of solids when cooling from the solidification temperature to ambient temperature [19]. The shrinkage induced a small error in the size which could be minimized by performing a structural compensation before the printing.

To further reduce the passband IL, a vibration grinding process was performed on the metal-printed filter. The fabricated filter was immersed in the vibration grinding machine tank filled with water and abrasive materials, as shown in Fig. 10(a). The inner and outer surfaces of the filter were polished. This improved the effective electrical conductivity of the 3-D printed aluminum alloy and thus decreased the associated conductor loss. The control of the polishing time was very important. Experiments showed that when the structure was grinded for too long, the improvement in the surface finish would not be as significant as at the beginning. Even worse, some critical geometries may be worn out, deteriorating the filter's RF performance. In this work, the filter was measured after 2 and 8 hours of polishing. The measured passband responses are plotted in Fig. 10(b) and compared with the one before the polishing. As can be seen, the measured passband IL of the filter is decreased with the increasing time of polishing. After 2 hours, the passband IL is reduced to around 0.5 dB. The IL is further reduced to around 0.33 dB after 8 hours, approaching the simulated IL value of 0.25 dB. Assuming all the loss is due to the roughness, the corresponding equivalent $R_q$ is improved to 1 μm. The measured $Q_u$ of the slotted spherical resonator is improved to be 4060, about 43% higher than the value before the polishing. The measured reflection response after polishing shows little difference from the one before polishing.

The EM-simulated and RF-measured frequency responses of the prototype II are compared in Fig. 11, showing much better agreement in terms of the passband IL and a negligible $\Delta f$, as compared with the metal 3-D printed prototype. In the passband, the measured average IL and minimum RL are 0.2 and 20 dB, respectively. The measured IL is only 0.05 dB higher than the simulated one. The measured $\Delta f$ is as small as 0.04% (4 MHz), indicating accurate reproduction of the structure. Noteworthy is that shrinkage also occurs in SLA process and can be induced by phase transformation of the resin from liquid to solid [20]. However, it is much less prominent because of the different materials and a high temperature is not involved in SLA process. As can be seen from Figs. 9(b) and 11(b), both filter prototypes demonstrate wide spurious-free stopbands with rejections over 20 dB up to 16.2 GHz. The first spurious passband appears beyond 17 GHz. Photographs of the fabricated filters are included in the insets of Figs. 9(b) and 11(b).

Fig. 12 shows the loss factor in the filters calculated by (1 - $|S_{11}|^2$ - $|S_{21}|^2$). This provides information on losses due to the metal as well as the radiation. It can be seen that at the higher spurious mode frequencies the loss is very high due to the enhanced radiation. Within the passband, the loss is mainly

caused by the conductor loss, and the loss (~0.2 dB) in the filter II is much smaller than the loss in the filter I (0.23–0.7 dB). This indicates a higher electrical conductivity of the plated copper than that of the aluminum alloy. Furthermore, within the passband the simulated loss difference between the non-slotted and slotted filters is less than 0.05 dB from Fig. 12(b), validating the negligible passband radiation. The impact of stopband radiation to external circuits can be mitigated by attaching microwave absorbers to the slots. The measured results of the filters with the absorbers attached show no significant difference to the one in Figs. 9 and 11 in terms of both the passband and the stopband responses. Finally, a comparison of the filters to previous related work is summarized in Table II. The filters reported here exhibit extended spurious-free stopbands compared to previous filters in [4], [5], and [8]. The proposed method of slotting can be extrapolated to higher order filters with flexible slot patterns to further enhance the stopband performance.

## VI. CONCLUSION

A high-$Q$ slotted spherical resonator is proposed to suppress spurious passbands of the BPF. The spurious $TM_{211}$ and $TE_{101}$ modes are eliminated, and an extended spurious-free stopband ($f_1/f_0$ > 1.7:1) is realized without significantly compromising the RF performance of the fundamental-mode passband. The filters made by two 3-D printing techniques, i.e., SLM and SLA, demonstrate good process flexibility. The excellent passband performance of the fabricated filters validates the capability of the utilized 3-D printing process for microwave waveguide devices.

## REFERENCES

[1] G. F. Craven and C. K. Mok, "The design of evanescent mode waveguide bandpass filters for a prescribed insertion loss characteristic," *IEEE Trans. Microw. Theory Techn.*, vol. MTT-19, no. 3, pp. 295–308, Mar. 1971.

[2] S. Amari, "Application of representation theory to dual-mode microwave bandpass filters," *IEEE Trans. Microw. Theory Techn.*, vol. 57, no. 2, pp. 430–441, Feb. 2009.

[3] R. J. Cameron and J. D. Rhodes, "Asymmetric realizations for dual-mode bandpass filters," *IEEE Trans. Microw. Theory Techn.*, vol. MTT-29, no. 1, pp. 51–58, Jan. 1981.

[4] C. Guo, X. Shang, M. J. Lancaster, and J. Xu, "A 3-D printed lightweight X-band waveguide filter based on spherical resonators," *IEEE Microw. Compon. Lett.*, vol. 25, no. 7, pp. 442–444, Jul. 2015.

[5] C. Guo, X. Shang, J. Li, F. Zhang, M. J. Lancaster, and J. Xu, "A lightweight 3-D printed *X*-band bandpass filter based on spherical dual-mode resonators," *IEEE Microw. Compon. Lett.*, vol. 26, no. 8, pp. 568–570, Aug. 2016.

[6] P. A Booth and E. V. Lluch, "Enhancing the performance of waveguide filters using additive manufacturing," *Proc. IEEE*, vol. 105, no. 4, pp. 613–619, Apr. 2017.

[7] P. A Booth and E. V. Lluch, "Realising advanced waveguide bandpass filters using additive manufacturing," *IET Microw., Antennas Propag.*, vol. 11, no. 14, pp. 1943–1948, 2017.

[8] J. Li, C. Guo, L. Mao, J. Xiang, G.-L. Huang, and T. Yuan, "Monolithically 3-D printed hemispherical resonator waveguide filters with improved out-of-band rejections," *IEEE Access*, vol. 6, no. 1, pp. 57030–57048, Oct. 2018.

[9] A. I. Dimitriadis, T. Debogović, M. Favre, M. Billod, L. Barloggio, J.-P. Ansermet, and E. de Rijk, "Polymer-based additive manufacturing of high-performance waveguide and antenna components,'' *Proc. IEEE*, vol. 105, no. 4, pp. 668–676, Apr. 2017.

[10] O. A. Peverini, G. Addamo, R. Tascone, G. Virone, P. Cecchini, R. Mizzoni, F. Calignano, E. P. Ambrosio, D. Manfredi, and P. Fino, "Enhanced topology of *E*-plane resonators for high-power satellite applications," *IEEE Trans. Microw. Theory Techn.*, vol. 63, no. 10, pp. 3361–3373, Oct. 2015.

[11] O. A. Peverini, G. Addamo, M. Lumia, G. Virone, F. Calignano, M. Lorusso, D. Manfredi, "Additive manufacturing of Ku/K-band waveguide filters: a comparative analysis among selective-laser melting and stereolithography," *IET Microw., Antennas Propag.*, vol. 11, no. 14, pp. 1936–1942, Nov. 2017.

[12] G.-L. Huang, C.-Z. Han, W. Xu, T. Yuan, and X. Zhang, "A compact 16-way high-power combiner implemented via 3-D metal printing technique for advanced radio-frequency electronics system applications," *IEEE Trans. Ind. Electron.*, vol. 66, no. 6, pp. 4767–4776, Jun. 2019.

[13] G.-L. Huang, S.-G. Zhou, C.-Y.-D. Sim, T.-H. Chio, and T. Yuan, "Lightweight perforated waveguide structure realized by 3-D printing for RF applications," *IEEE Trans. Antennas Propag.*, vol. 65, no. 8, pp. 3897–3904, Aug. 2017.

[14] G. Addamo, O. A. Peverini, D. Manfredi, F. Calignano, F. Paonessa, G. Virone, R. Tascone, and G. Dassano, "Additive manufacturing of Ka-band dual-polarization waveguide components," *IEEE Trans. Microw. Theory Techn.*, vol. 66, no. 8, pp. 3589–3596, Aug. 2018.

[15] O. A. Peverini, M. Lumia, G. Addamo, F. Paonessa, G. Virone, R. Tascone, F. Calignano, G. Cattano, and D. Manfredi, "Integration of an *H*-plane bend, a twist, and a filter in Ku/K-band through additive manufacturing," *IEEE Trans. Microw. Theory Techn.*, vol. 66, no. 5, pp. 2210–2219, May 2018.

[16] CST Computer Simulation Technology AG., USA (Jul. 2018). [Online]. Available: www.cst.com.

[17] J. S. Hong and M. J. Lancaster, *Microstrip Filters for RF/Microwave Applications*. New York, USA: Wiley, 2001.

[18] Accura® Xtreme™, 3D Systems, Inc., USA (Sept. 2018). [Online]. Available: www.3dsystems.com.

[19] H. H. Zhu, L. Lu, and J. Y. H. Fuh, "Study on shrinkage behaviour of direct laser sintering metallic powder," *Proc. Inst. Mech. Eng. B J. Eng. Manuf.*, vol. 220, 2006.

[20] W. L. Wang, C. M. Cheah, J. Y. H. Fuh, and L. Lu, "Influence of process parameters on stereolithography part shrinkage," *Mater. Des.*, vol. 17, no. 4, pp. 205–213, 1996.